# Compact, Flexible Harmonic Transponder Sensor With Multiplexed Sensing Capabilities for Rapid, Contactless Microfluidic Diagnosis

Liang Zhu<sup>10</sup>, Graduate Student Member, IEEE, Haiyu Huang, Member, IEEE, Mark Ming-Cheng Cheng, and Pai-Yen Chen<sup>10</sup>, Senior Member, IEEE

Abstract-In this article, we design and experimentally demonstrate a flexible, low-profile harmonic transponder sensor, capable of performing multiplexed fluidic sensing. The harmonic transponder comprises multiple reconfigurable electrically small antennas (ESAs) integrated with microfluidic channels for receiving radio frequency (RF) signals at the fundamental frequencies  $(f_0)$ , as well as a broadband microstrip monopole for retransmitting the second-harmonic signal (2  $f_0$ ) to a sniffer. Such a frequency orthogonality can help suppressing possible echoes, clutters, and crosstalks in the rich-scattering environment. We show that injection of different liquid samples into a microfluidic channel, which tunes the operating frequency of an ESA, can be precisely recognized by analyzing the shift of peak second-harmonic received signal strength indicator (RSSI) in the frequency-hopping spread spectrum (FHSS). We also demonstrate the possibility of performing rapid and multiplexed noncontact detection with the proposed harmonic transponder sensor. We envision that this battery-free and lightweight multiplexing wireless sensor may benefit various Internet-of-Things (IoTs) and healthcare applications, such as rapid contactless point-of-care (POC) and drive-through tests.

Index Terms—Contactless test, electrical small antenna (ESA), electromagnetic interferences, fluidic channel, harmonic radar, harmonic sensors, metamaterial-inspired antenna, passive wireless sensors, point-of-care (POC).

#### I. INTRODUCTION

N THE past decade, with the rapid development of Internetof-Things (IoTs) and smart devices, the power-saving wireless sensing techniques have drawn rapidly growing interest because the integration of wireless communication networks with sensor nodes can provide significant advantages in terms of high data rate, real-time monitoring, and the capability to synchronously upload information for the cloud-based data analysis [1], [2]. The first generation of wireless smart sensors

Manuscript received April 24, 2020; revised June 15, 2020; accepted June 18, 2020. Date of publication July 9, 2020; date of current version November 4, 2020. This work supported by the National Science Foundation through the ECCS-CCSS Program under Grant 1914420. (Corresponding author: Pai-Yen Chen.)

Liang Zhu and Pai-Yen Chen are with the Department of Electrical and Computer Engineering, University of Illinois at Chicago, Chicago, IL 60607 USA (e-mail: pychen@uic.edu).

Haiyu Huang is with Maxim Integrated Inc., Dallas, TX 75254 USA. Mark Ming-Cheng Cheng is with the Department of Electrical and Com-

puter Engineering, The University of Alabama, Tuscaloosa, AL 35487 USA. Color versions of one or more of the figures in this article are available online at http://ieeexplore.ieee.org.

Digital Object Identifier 10.1109/TMTT.2020.3006286

can be dated back to 2000 (e.g., wireless pressure sensing [3]), and ever since then, it has been widely demonstrated in monitoring the environment parameters [4], biological parameter [5], humidity [6], and temperature [7], to name a few. However, to date, most of the wireless devices are active devices; namely, they usually need an external power source, such as a battery or an energy harvester, which inevitably adds a significant amount of complexity and error sources to the system [8]. To enhance the system's durability and robustness, and to reduce maintenance costs, many battery-free wireless sensors have been developed, which, in principle, can be divided into two categories. The first type is based on the near-field inductive/capacitive coupling mechanism, which has been demonstrated to be effective for versatile LC-based biomedical sensors [9]–[13] and capacitive pressure or humidity detectors [3], [14], [15]. However, this near-field coupling scheme has the commonly known disadvantages of short interrogation distance that is limited to several inches; this poses an inconvenience for practical sensing applications. To overcome such limitations, electromagnetic backscattering techniques have been exploited to perform long-distance wireless sensing. In this manner, microstrip antenna sensors and passive radio frequency identification (RFID) have been proposed for remotely detecting environmental changes [16]–[18]. Unfortunately, even though such systems could have longer interrogation distance, backscatter sensors are usually vulnerable to direct coupling, scattering interferences, and clutters surrounding them.

Compact, passive harmonic sensors are gaining increasing attention. Similar to a harmonic radar [19] that has been successfully used in tracking objects with a very small radar cross section (RCS) [20]–[22], a harmonic sensor launches and detects orthogonal harmonics to avoid multiple interferences, clutters, and crosstalks between  $T_x$  and  $R_x$  [23]–[25]. These harmonic sensors have been extended to remote sensing of strain and cracks [26], [27], humidity sensing [28], localization of underground buried assets [29]–[31], and noninvasive detection of critical symbols in healthcare applications [32]–[35]. Especially, facing the crisis of global aging and pandemic (e.g., COVID-19) [36], rapid, low-cost, and disposable point-of-care (POC) tests and drive-through tests are in exponentially growing demands. Recently, we have proposed a passive harmonic transponder hybridized with an antenna sensor for monitoring

0018-9480 © 2020 IEEE. Personal use is permitted, but republication/redistribution requires IEEE permission. See https://www.ieee.org/publications/rights/index.html for more information.

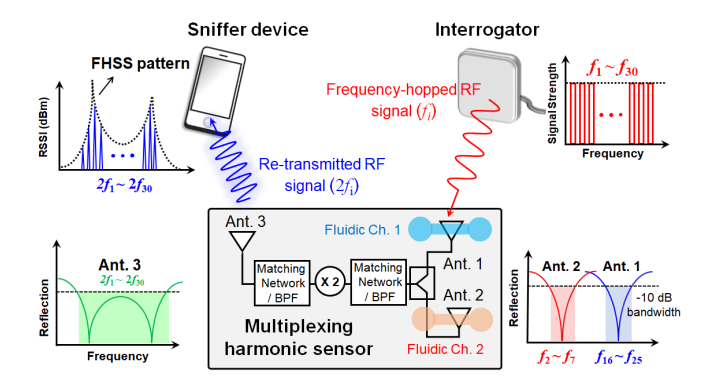


Fig. 1. Schematics of the integrated harmonic sensor based on microstrip antennas, where antennas Ant. 1 and Ant. 2 exhibit a liquid-reconfigured resonance at the fundamental frequency  $f_0$ , and antenna Ant. 3 exhibits insensitive wideband resonance centering in the second-harmonic band  $2f_0$ . The full-passive harmonic sensor receives and backscatters the RF signals at orthogonal frequencies, so as to avoid clutters, multipath interferences, and crosstalks. The type of liquid droplets in each fluidic channel can be retrieved by analyzing the FHSS patterns of the recorded second harmonic signals.

liquid levels in medical and healthcare applications [37], [38]. This technique is based on the harmonic received signal strength indicator (RSSI) data under the FHSS of UHF RFID signals, which is particularly suitable for convenient POC and drive-through tests. In fact, the already popularly deployed RFID toll tag readers can be used as interrogators, and healthcare workers can use smartphones as data sniffers/decoders for drive-through tests. Such a contactless, wireless sensing platform will not only drastically improve the throughput but also reduce the risk for the healthcare workers if testing with contagious diseases. Although the existing harmonic transponder sensors have several advantages in healthcare and IoT applications, they have certain intrinsic limitations. As an example, they generally lack the ability to simultaneously cope with multiple test channels or multiple test parameters [39]–[41], which may not satisfy the complexity requirement of many healthcare applications in practice. Another limitation is the lack of good mechanical flexibility and compactness, which further limits the applications of these harmonic sensors in the fields of wearable and textile electronics. For example, harmonic-based antenna sensors in [40] and [41] were based on semirigid, dual-, or multimode microstrip patch antennas (i.e., cavities with open sidewalls), of which only a specific cavity mode is perturbed by the dielectric loading, while others remain unchanged. Considering the complicated modal profile in a compact cavity, it is rather difficult to design a multiplexing sensor.

We herein propose a lightweight and flexible multiplexing harmonic transponder sensor, which allows for rapid, in situ detection of at least two types of liquid samples. As sketched in Fig. 1, the system consists of a transceiver  $(T_x)$  that transmits a constant-strength frequency-hopping sequence with totally 30 channels  $[f_1, f_2, ..., f_{30}]$  to the multiplexing harmonic sensor. The frequency-hopped radio frequency (RF) signal is received by the sensor's electrical small antennas (ESAs), with strength modulated by the sample under test (SUT) in the fluidic channels. The received

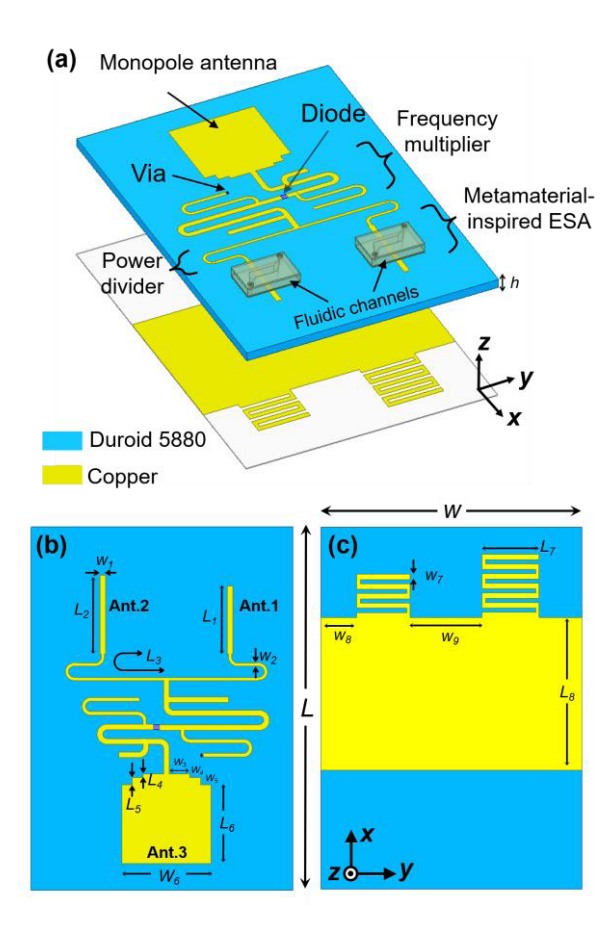


Fig. 2. Schematics and dimensions of a compact, fully passive harmonic transponder comprising two ESAs integrated with separate fluidic channels, a frequency multiplier, a power divider, and a broadband monopole antenna. (a) 3-D view, (b) top view, and (c) bottom view of this duplex harmonic

RF signals then undergoes frequency doubling (i.e.,  $[f_1, f_2, \ldots, f_{30}] \rightarrow [2f_1, 2f_2, \ldots, 2f_{30}]$ ) and is retransmitted to the sniffers. Finally, the dielectric property of the SUT can be retrieved by postprocessing the high-dimensional frequency-hopping spread spectrum (FHSS) pattern  $[2f_1, 2f_2, \ldots, 2f_{30}]$ . We should emphasize that the proposed harmonic sensor can be generalized into a multiplexed sensing platform that can simultaneously monitor several SUTs, with good isolation and ignorable mutual coupling. The proposed technique may be of interest for emerging wearable, textile, and implantable electronic devices. In the following, we will discuss the design and practical implementation of this flexible, fully passive multiplexing harmonic sensor used for contactlessly sensing two binary mixtures in the far zone.

## II. DESIGN AND MEASUREMENT OF HARMONIC TRANSPONDERS

Fig. 2(a) illustrates the 3-D geometry of the proposed harmonic transponder, which comprises two metamaterial-inspired ESAs [42]–[44], a power divider, a passive frequency multiplier, and a rectangular monopole antenna with their optimal design parameters as summarized in Table I. The metamaterial-inspired ESAs are typically composed of *LC* resonant structures that are inspired by the design of the unit

TABLE I
SUMMARY OF DIMENSIONS IN THE HARMONIC TAG (UNIT: MILLIMETERS)

Par.	L	W	$L_1$	$L_2$	$L_3$	$L_4$	$L_5$	$L_6$	$L_7$	$L_8$
Value	100	70	19	22	42	1	2	22	16	43
Par.	$W_I$	$W_2$	$W_3$	$W_4$	$W_5$	$W_6$	$W_7$	$W_8$	$W_9$	
Value	1.58	0.85	5.7	3	3	25	1.5	10	20	

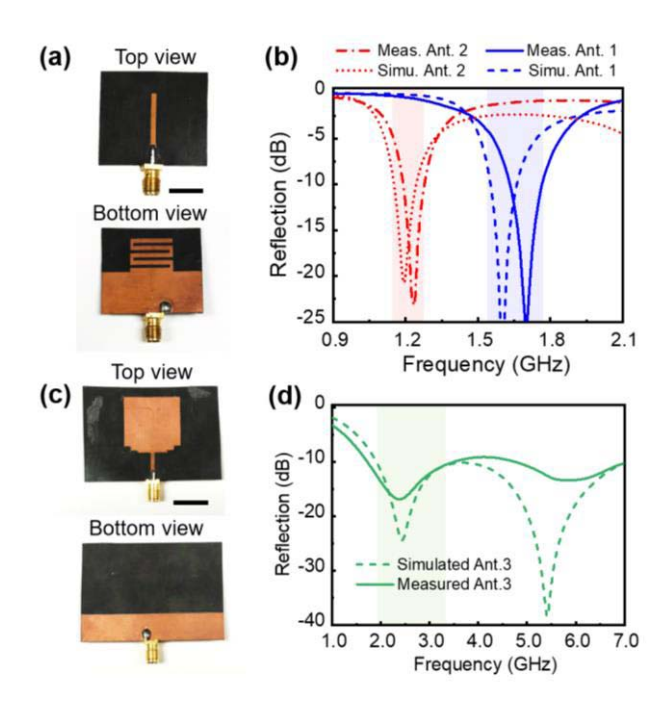


Fig. 3. (a) Photographs and (b) measured reflection coefficient for the metamaterial-inspired ESAs (Ant. 1). (c) and (d) Similar to (a) and (b), but for the wideband monopole antenna. The scale bar in (a) and (c) are 1.5 and 2 cm, respectively.

cell (or metaatom) [45]–[48] constituting the metamaterial. Therefore, when compared with metamaterial-based ESAs, the metamaterial-inspired ESAs can be more readily designed and physically implemented. Here, the metamaterial-inspired ESAs (Ant.1 and Ant. 2 in Fig. 1) used for receiving fundamental tones comprise a short stub and a grounded meander line. The inductive nature of a meander-line metaatom [42] can compensate for the capacitive nature of a short monopole, thus forming a resonant radiating system matched to a 50- $\Omega$  input impedance, without any matching components or stubs. The generated second harmonics are retransmitted by a wideband rectangular monopole antenna (Ant. 3 with a 50- $\Omega$  input impedance in Fig. 1) to the sniffer/reader. The two layers of the harmonic transponder are separated by the Rogers 5880 substrate with relative permittivity  $\varepsilon_r = 2.2$ , loss tangent  $\delta = 0.0009$ , and thickness d = 0.508 mm. In this work, commercial software, ANSYS High Frequency Structure Simulator (HFSS), was used for simulation and optimization of the proposed antennas [49]. The Advanced Design Simulator (ADS) was used for the design of the power divider and the frequency multiplier [50]. Fig. 3 presents the photographs and the measured reflection spectra for these three antennas. The results in Fig. 3(b) show that the two narrowband ESAs resonate at 1.23 and 1.73 GHz, with a

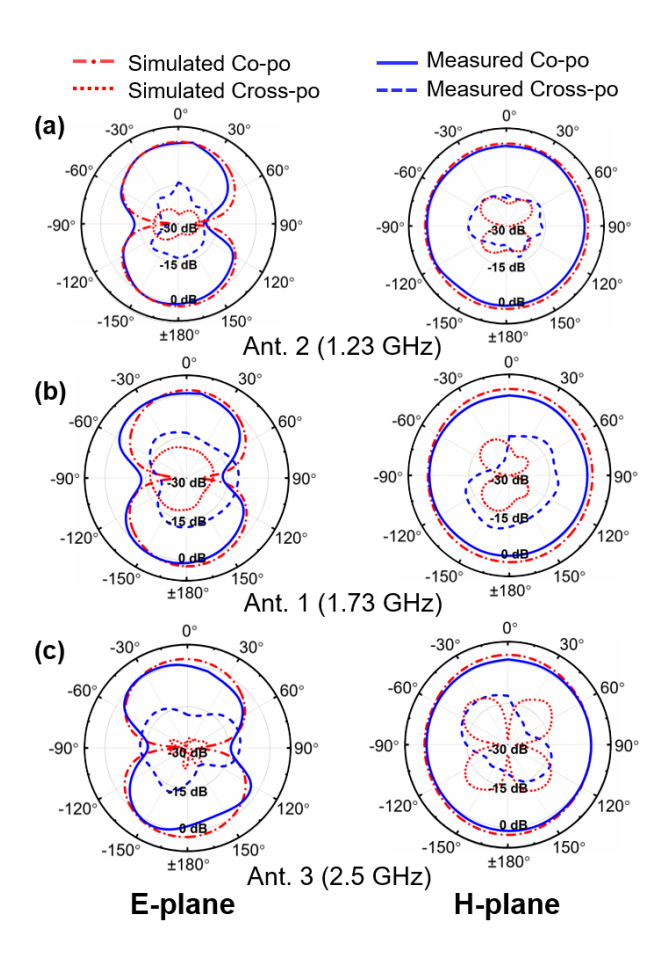


Fig. 4. Radiation patterns for (a) Ant. 2 at 1.23 GHz, (b) Ant. 1 at 1.73 GHz, and (c) Ant. 3 at 2.5 GHz.

bandwidth of 130 and 160 MHz, respectively. The rectangular microstrip monopole antenna exhibits a wideband resonance (2–6 GHz), covering the entire second-harmonic spectrum of the two ESAs, as shown in Fig. 3(d). The measurement and simulation results are in a good agreement, with the percentage frequency up-shift 6.5% for Ant. 1 and 4% for Ant. 2, due to fabrication errors and variations in the permittivity of the substrate.

Fig. 4 reports the radiation patterns on the E(x-z) and H(y-z) planes for the three antennas in Fig. 3 at the operating frequency (1.23, 1.73, and 2.5 GHz). Both the measured and simulated results show that the proposed antennas exhibit omnidirectional radiation properties with linear polarizations. The measured maximum gains for Ant. 1, Ant. 2, and Ant. 3 are 2, 1.8, and 2.1 dBi, respectively. The measurement results agree quite well with the simulated ones, as can be seen from Fig. 4. We also note that for all the three antennas, the crosspolarization patterns are lower than -15 dB on the E- and H-planes, when compared with their co-polarization patterns.

These antennas are integrated with a passive frequency multiplier [Fig. 5] and a power divider [Fig. 6] for building a passive harmonic transponder. The schematic and the photograph of the passive frequency multiplier are presented in Fig. 5(a) and (b), respectively, of which the shunt quarter-wavelength ( $\lambda_0/4$ ) short-circuited and open-circuited

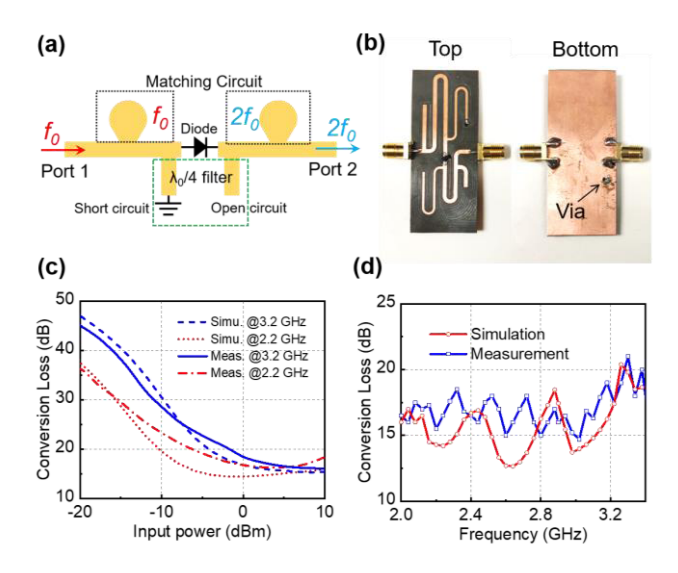


Fig. 5. (a) Circuit schematic and (b) implementation of a compact passive frequency multiplier, and its simulated and measured conversion loss in (c) as a function of input power and in (d) at different output frequencies.

stubs are placed around a Schottky diode (HSMS 2850). At  $f_0$  $(2f_0)$ , the  $\lambda_0/4$  short-circuited stub is an open (short) end at its input, whereas the open-circuited stub behaves like a short (open) end. Consequently, the injected RF signal at  $f_0$  passes through the input matching network and reaches out to the diode, while the quarter-wavelength open-circuited stub (at  $f_0$ ) at the output shorts the fundamental tone. Fig. 5(c) reports the measurement result for the conversion loss of the passive frequency multiplier in Fig. 5(b) at different input power levels. We find that at 0-dBm input level, the minimum conversion loss is  $\sim$ 15 dB at 2.2 GHz and is  $\sim$ 17 dB at 3.2 GHz. Fig. 5(d) reports the frequency dependence of this diode-based frequency multiplier at 0-dBm input power level, showing that within the frequency band of interest (2.0–3.4 GHz), the frequency doubling efficiency is fairly constant, with a less than 5-dB fluctuation. We note that the bandwidth and conversion loss flatness of the frequency multiplier can be improved by replacing tuning stubs with lumped-element matching networks and filters. Moreover, this work focuses mainly on demonstrating a proof-of-concept prototype and the FHSS sensing scheme. Nevertheless, by scaling the device and circuit appropriately, the concept can be applied to any frequency band of interest. Fig. 6(a) shows the photograph of the fabricated power divider, where two quarter-wavelength transformers with characteristic impedance  $\sqrt{2}$   $Z_0 = 70.7\Omega$ are in parallel to each other, to equally separate or combine RF powers. The simulated and measured S-parameters of this power divider are presented in Fig. 6(b), showing that the reflection coefficient  $(S_{11})$  is lower than -20 dB over the frequency band 1–1.5 GHz, and the transmission coefficients  $(S_{21} \text{ and } S_{31})$  are  $\sim -3$  dB within the same frequency range, with a good amplitude consistency ( $|S_{21} - S_{31}| < 0.3 \text{ dB}$ ).

## III. MICROFLUIDICS-INTEGRATED MULTIPLEXING HARMONIC SENSOR

By loading fluidic channels on the top of the resonant ESAs in the harmonic transponder, a battery-free harmonic sensor

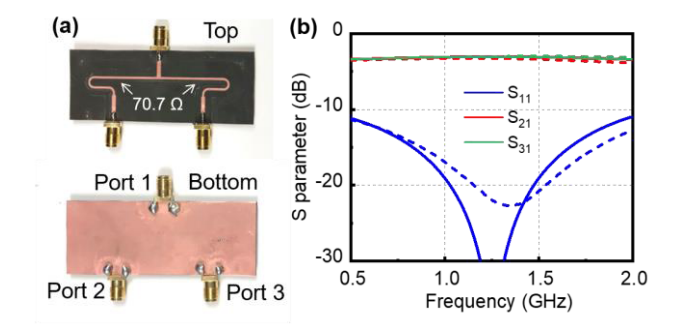


Fig. 6. (a) Top and bottom views of the fabricated power divider and (b) its simulated and measured insertion loss, return loss, and isolation. Solid and dashed lines represent the measurement and simulation results, respectively.

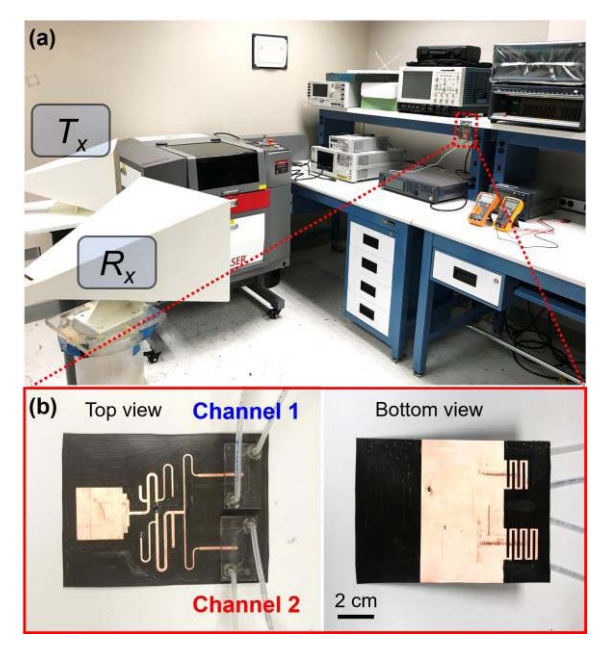


Fig. 7. (a) Bistatic measurement setup in an indoor environment. (b) Top and bottom views of the multiplexing harmonic sensor.

can be built, as schematically shown in Figs. 2 and 7. Here, we adopted the bistatic measurement configuration in a noisy indoor environment containing clutters, echoes, and interferences, as shown in Fig. 7(a). To avoid the crosstalk between the interrogator and the sniffer, the interrogator  $T_x$  was connected to a low-pass filter (DC-1.7 GHz) [51] and the sniffer  $R_x$  was connected to a bandpass filter (1.9-4.7 GHz) [52]. Fig. 7(b) presents the photograph of this multiplexing harmonic sensor, where plastic tubes are connected to the isolated fluidic channels to guide SUTs in and out. We prepared a binary mixture composed of acetone and water with different volume ratios: A/W = 100%, 66%, 33%, and 0% (which gives an (real-part) effective relative permittivity  $\varepsilon_r = 20.7, 32, 58, \text{ and } 80 [53]$ . In our measurements [Fig. 7(a)], the interrogator transmits a frequency-hopped RF signal to the harmonic sensor. The transmitter in the interrogator hops the carrier frequency every 2 s and totally 30 frequency channels are swept, with a resolution of 8 MHz. In practice, the frequency hopping rate could be several hundreds of hops per second. Synchronization

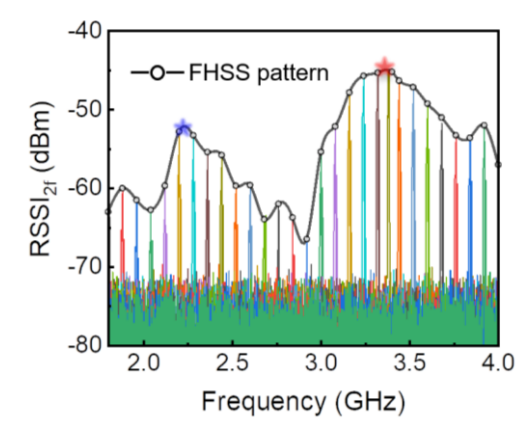


Fig. 8. Measured second-harmonic RSSI array of the multiplexing harmonic sensor in Fig. 7. The envelope of the RSSI array represents the FHSS pattern, which can be exploited to retrieve liquid properties in each fluidic channel. The licensed tones (e.g., 2.4-GHz WiFi router) in the ambient environment were excluded from the hopped carrier frequencies. Besides, those stationary and flickering peaks can be easily subtracted from the measured FHSS pattern.

between the interrogator and the sniffer is controlled by the LabVIEW program. Afterward, the nonlinear sensor doubles the frequency of the RF signal and resends the second harmonic to the  $R_x$  antenna or sniffer. The backscattered second-harmonic RSSIs measured by the sniffer form a unique FHSS pattern [see Fig. 8], whose peak frequency may be interrelated with the effective relative permittivity of the injected SUTs. The second-harmonic RSSI can be estimated using the Friis transmission equation [54]

$$\frac{P_r}{P_t} = \left(\frac{\lambda_0}{4\pi R_1}\right)^2 \times \left(\frac{\lambda_0/2}{4\pi R_2}\right)^2 \times \frac{G_r G_t G_R G_T}{L_{\text{sys}}} \tag{1}$$

where  $G_r$  is the realized gain of the ESAs at  $f_0$ ,  $G_t$  is the realized gain of the broadband monopole antenna at  $2f_0$ ,  $G_T$  $(G_R)$  denotes the realized gain of  $T_x$   $(R_x)$ ,  $R_1$   $(R_2)$  is the distance between  $T_x$  ( $R_x$ ) and the sensor, and  $L_{sys}$  is the system loss that includes the conversion loss of the frequency doubler [Fig. 5(c)], and dielectric/conduction losses in passive circuits and SUTs. Here, the important parameters for our measurement setup are as follows:  $P_t = 25$  dBm,  $R_1 = R_2 =$ 1 m,  $G_T = 10.5$  dBi at 1.4 GHz, and  $G_R = 16.5$  dBi at 2.8 GHz. Under a fixed transmitted power  $P_t$ , the received power  $P_r$  is sensitively responsible for changes in  $G_r$  (which could be caused by the variations in dielectric properties of the liquid solution filled in the fluid channels). According to the cavity perturbation theory [55], [56], the resonance frequency shift in response to the dielectric perturbations is proportional to the electric field strength of the perturbed mode. Since the fluidic channel is placed on the top of the microstrip feedline of the ESA where electric fields are strongly localized, any small increment in the dielectric constant of SUTs may greatly downshift the resonant frequency of the ESA [53], which, in turn, results in a visible downshift in the recorded FHSS pattern.

Fig. 9 presents the FHSS patterns measured at different interrogation distances in the indoor environment shown in Fig. 7; here, except for the sensor-to-sniffer distance  $(R_2)$ ,

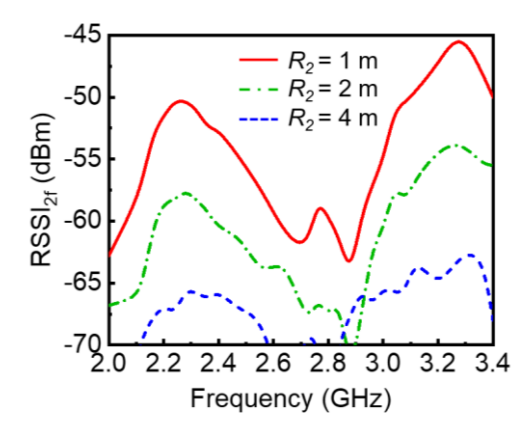


Fig. 9. FHSS pattern of the multiplexing harmonic sensor at different interrogating distances.

all the measurement conditions remain the same. It is evidently seen that the peak frequency in the FHSS pattern remains unchanged, regardless of the interrogation range. Therefore, the FHSS pattern analysis provides an absolute accuracy sensing with high robustness and reliability. This is, however, impossible for a typical passive harmonic tag that detects the RSSI amplitude at a constant operating frequency. In addition, the redundant information from extra dimensions can tolerate the variation in other factors, such as the sensor location and interferences from near-field objects. The maximum detection range is ~4.0 m for a given noise floor of -70 dBm. The maximum range is expected to be increased by adjusting configurations of the spectrum analyzer with reduced noise floor and/or by optimizing antennas and circuits used in the harmonic tag.

Next, to demonstrate the multiplexed sensing capability of the proposed wireless sensor, we have conducted sensing experiments for three different scenarios, which are as follows: (A) Channel 1 is filled with the SUT and Channel 2 is empty; (B) Channel 1 is empty, and Channel 2 is filled with the SUT; and (C) both fluidic channels are filled with SUTs. Here, the important parameters used in this measurement setup are as follows:  $P_t = 25 \text{ dBm}$ ,  $R_1 = R_2 = 1.3 \text{ m}$ ,  $G_T = 10.5 \text{ dBi}$ at 1.4 GHz,  $G_R = 16.5$  dBi at 2.8 GHz, and the liquid volume of SUT is set to 100  $\mu$ L (i.e., the total volume of the fluidic channel). Fig. 10 reports the measurement results for the sensing scenario A. It is seen from Fig. 10(a) that by injecting acetone-water mixtures of different concentrations into Channel 1, the first RSSI peak in the FHSS pattern can be shifted from 2.28 to 2.07 GHz, whereas the second RSSI peak is locked at 3.25 GHz, as summarized in Fig. 10(b). On the other hand, for scenario B, the first RSSI peak remains unchanged, whereas the second RSSI peak is downshifted from 3.11 to 2.6 GHz, as can be seen from Fig. 11(a) and (b). The measured results in Figs. 10 and 11 clearly indicate that multiplexed sensing with good isolation may be possible with the proposed compact, fully passive harmonic sensor. Fig. 12 reports the measurement results for the sensing scenario C, where the harmonic sensor is exploited to simul-

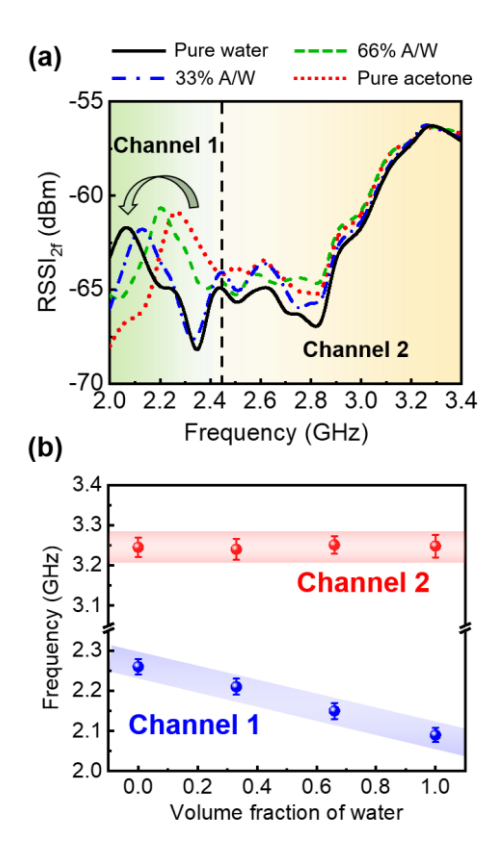


Fig. 10. (a) Measured FHSS pattern of the multiplexing harmonic sensor, of which Channel 1 is injected with SUT and Channel 2 is empty (sensing scenario A). (b) Peak frequency extracted from the FHSS pattern for different volume fractions of water in the acetone–water mixture.

taneously monitor two SUTs. It is seen from Fig. 12 that when acetone-water mixture of different concentrations are injected into the two fluidic channels, the first RSSI peak is shifted from 2.27 to 2.09 GHz. Besides, the second one is also shifted from 3.12 to 2.61 GHz. Such results further confirm robustness and multiplexed sensing ability of the proposed harmonic sensor in noisy environments. For different injected SUTs, the peak RSSI strength may slightly change because the dielectric constants and loss tangents of them could be different. The loss tangent fitted from the measurement result is 0.025 for pure acetone and 0.04 (0.055) for the mixture with A/W = 66% (33%) and is increased to 0.075 for pure water. Increasing the SUT's dielectric loss (i.e., increase the volume fraction of water) may decrease the quality factor (Q-factor) of the ESA, which in turn reduces the peak RSSI value and increases the linewidth of the FHSS pattern, as can be seen from Figs. 10-12.

Finally, we notice that this harmonic sensor was manufactured using a single-layer Rogers 5880 substrate with a thickness of only 0.5 mm, thus allowing good flexibility. We have deployed the flexible harmonic tag on an empty dielectric tube [polyvinyl chloride (PVC) pipe with radius  $r=10~{\rm cm}$  and relative permittivity  $\varepsilon_r=2.3$  at 2.6 GHz], as shown in Fig. 13(a) and (b). In this case, the tag has a  $\pm 30^{\circ}$  bending angle, and the injected liquid volume is  $100~{\mu}{\rm L}$ . The same bistatic telemetry setup was used to measure the FHSS patterns

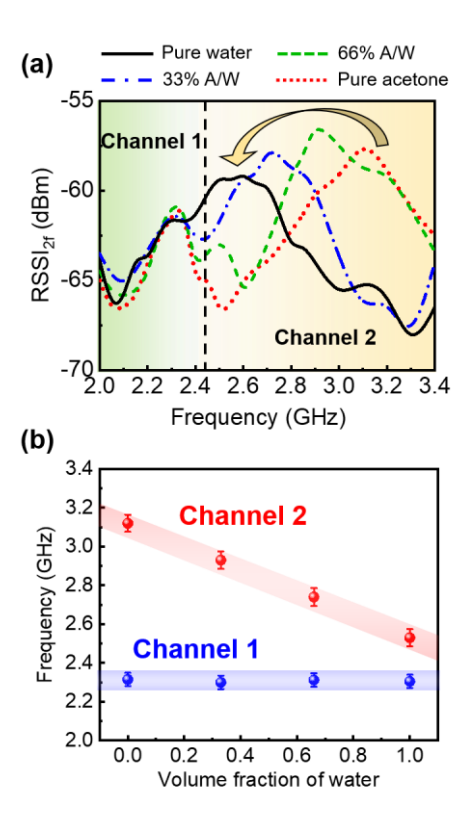


Fig. 11. (a) and (b) Similar to Fig. 9(a) and (b), but for the sensing scenario B where Channel 2 is injected with the acetone–water mixture of different concentrations and Channel 1 is void.

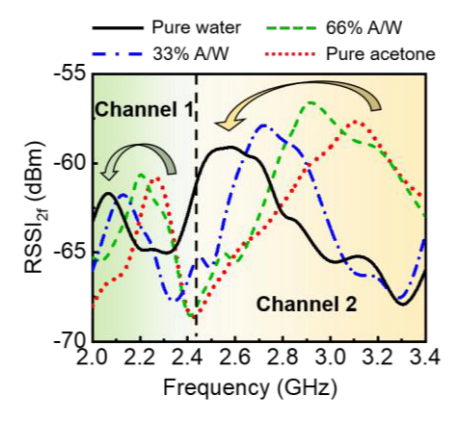


Fig. 12. Similar to Fig. 9, but for the sensing scenario C, where both fluidic channels are filled with mixtures of different concentrations.

of the harmonic tag attached conformally to the PVC tube. Fig. 13(c) reports the normalized peak frequency extracted from the FHSS patterns for water–acetone mixtures with different water volume fractions; here, three different bending angles were tested. From Fig. 13(c), it is seen that bending the harmonic tag does not affect the sensing performance, which once again proves the robustness of our prototype in withstanding a moderate range of bends. The sensitivity and resolvability of the proposed device can be defined as the slope of the peak RSSI frequency versus the water volume fraction [see Fig. 13(c)], which are obtained as 2.1 MHz/1% for Channel 1 and 5.1 MHz/1% for Channel 2. Such results

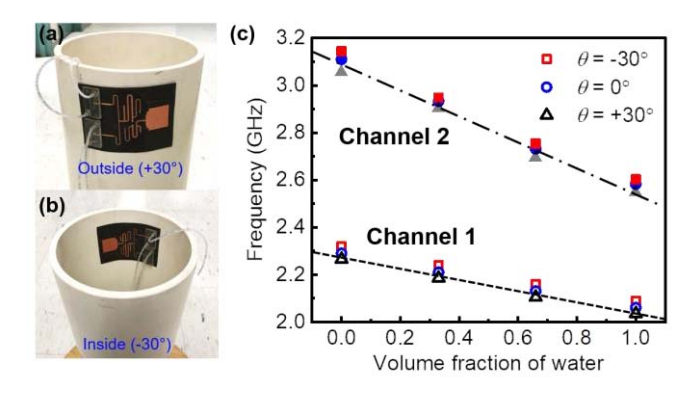


Fig. 13. Conformal multiplexing harmonic tags attached to a dielectric tube at a bending angle approximately equal to (a)  $+30^{\circ}$  and (b)  $-30^{\circ}$ . (c) Peak frequency of the FHSS patterns against the volume fraction of water in the acetone–water mixture for sensing scenario C (the results for  $\theta=0^{\circ}$  can be seen from Fig. 11).

suggest that for a 100- $\mu$ L microfluidic reservoir,  $\pm 1\%$  change in the volume fraction of water may be detected using a standard spectrum analyzer with a 10-kHz resolution bandwidth. As an example, the flexible harmonic tag can be deployed on the PVC pipes in the plumbing system [see Fig. 13(a)], for which plastic tubes can guide SUTs from different nodes into specific channels. In addition, a plastic tube carrying environmental mixtures (e.g., water mixed with microplastics, microfibers, detergents, and hydrogen peroxides) can be connected to microfluidic separation and sorting cells for delivering a specific SUT to its assigned channel. In general, the ratio of dielectric constant between these agents and pure water is greater than that between acetone and water. Ideally, an array of narrow-band ESA and liquid channels can be realized for multiplexed sensing purposes. We should point out that this conformal wireless sensor with high sensitivity and good linearity may have potential applications in healthcare, medical, and biological monitoring systems, such as the labon-a-chip and POC, as well as industrial and environmental monitoring, such as oil tube crack detection or water tube leakage monitoring. The SUT is not limited to acetone-water mixtures, but can also be extended to a variety of widely used solutions, such as ethanol-water and glucose-water.

### IV. CONCLUSION

We have demonstrated a compact, low-profile, and fully passive harmonic transponder with the scalable and multiplexed sensing capability. By hybridizing this harmonic transponder with microfluidic channels, we have built a zero-power multiplexing harmonic sensor and have demonstrated its ability to rapidly and contactlessly monitor properties of aqueous solutions in a noisy indoor environment. Comparing to the traditional linear backscatter RFID tags, the proposed harmonic-based telemetry configuration may offer enhanced robustness and reliability in real-world applications. We envision that such multiplexing harmonic tags may be integrated with system-level microfluidic networks (e.g., sorting cells and diagnostic assays) to maximize its potential for wireless sensing and

telemetering, lab-on-a-chip measurements, rapid healthcare tests (e.g., POC tests and drive-through tests), Industry 4.0, and IoTs.

#### REFERENCES

- [1] S. Amendola, R. Lodato, S. Manzari, C. Occhiuzzi, and G. Marrocco, "RFID technology for IoT-based personal healthcare in smart spaces," *IEEE Internet Things J.*, vol. 1, no. 2, pp. 144–152, Apr. 2014.
- [2] G. Bedi, G. K. Venayagamoorthy, R. Singh, R. R. Brooks, and K.-C. Wang, "Review of Internet of Things (IoT) in electric power and energy systems," *IEEE Internet Things J.*, vol. 5, no. 2, pp. 847–870, Apr. 2018.
- [3] K. G. Ong and C. A. Grimes, "A resonant printed-circuit sensor for remote query monitoring of environmental parameters," *Smart Mater. Struct.*, vol. 9, no. 4, pp. 421–428, Aug. 2000.
- [4] K. Ghee Ong, K. Zeng, and C. A. Grimes, "A wireless, passive carbon nanotube-based gas sensor," *IEEE Sensors J.*, vol. 2, no. 2, pp. 82–88, Apr. 2002.
- [5] J. Coosemans, M. Catrysse, and R. Puers, "A readout circuit for an intraocular pressure sensor," Sens. Actuators A, Phys., vol. 110, nos. 1–3, pp. 432–438, Feb. 2004.
- [6] Y. Feng, L. Xie, Q. Chen, and L.-R. Zheng, "Low-cost printed chipless RFID humidity sensor tag for intelligent packaging," *IEEE Sensors J.*, vol. 15, no. 6, pp. 3201–3208, Jun. 2015.
- [7] J. Tan et al., "A fully passive RFID temperature sensor SoC with an accuracy of ±0.4 oC (3σ) from 0 oC to 125 oC," IEEE J. Radio Freq. Identif., vol. 3, no. 1, pp. 35–45, Mar. 2019.
- [8] D. Dondi, A. Bertacchini, D. Brunelli, L. Larcher, and L. Benini, "Modeling and optimization of a solar energy harvester system for selfpowered wireless sensor networks," *IEEE Trans. Ind. Electron.*, vol. 55, no. 7, pp. 2759–2766, Jul. 2008.
- [9] P. Y. Chen et al., "Generalized parity-time symmetry condition for enhanced sensor telemetry," Nat. Electron., vol. 1, pp. 297–304, May 2018.
- [10] P.-J. Chen, S. Saati, R. Varma, M. S. Humayun, and Y.-C. Tai, "Wireless intraocular pressure sensing using microfabricated minimally invasive flexible-coiled LC sensor implant," *J. Microelectromech. Syst.*, vol. 19, no. 4, pp. 721–734, Aug. 2010.
- [11] L. Y. Chen et al., "Continuous wireless pressure monitoring and mapping with ultra-small passive sensors for health monitoring and critical care," Nature Commun., vol. 5, no. 1, p. 5028, Dec. 2014.
- [12] M. Sakhdari, M. Hajizadegan, Q. Zhong, D. N. Christodoulides, R. El-Ganainy, and P.-Y. Chen, "Experimental observation of PT symmetry breaking near divergent exceptional points," *Phys. Rev. Lett.*, vol. 123, no. 19, Nov. 2019, 193901.
- [13] P.-Y. Chen and R. El-Ganainy, "Exceptional points enhance wireless readout," *Nature Electron.*, vol. 2, no. 8, pp. 323–324, Aug. 2019.
- [14] Q.-A. Huang, L. Dong, and L.-F. Wang, "LC passive wireless sensors toward a wireless sensing platform: Status, prospects, and challenges," *J. Microelectromech. Syst.*, vol. 25, no. 5, pp. 822–841, Oct. 2016.
- [15] T. J. Harpster, B. Stark, and K. Najafi, "A passive wireless integrated humidity sensor," Sens. Actuators A, Phys., vol. 95, nos. 2–3, pp. 100–107, Jan. 2002.
- [16] L. Yang, A. Rida, R. Vyas, and M. M. Tentzeris, "RFID tag and RF structures on a paper substrate using inkjet-printing technology," *IEEE Trans. Microw. Theory Techn.*, vol. 55, no. 12, pp. 2894–2901, Dec. 2007.
- [17] L. Yang, R. Zhang, D. Staiculescu, C. P. Wong, and M. M. Tentzeris, "A novel conformal RFID-enabled module utilizing inkjet-printed antennas and carbon nanotubes for gas-detection applications," *IEEE Antennas Wireless Propag. Lett.*, vol. 8, pp. 653–656, 2009.
- [18] B. S. Cook, J. R. Cooper, and M. M. Tentzeris, "An inkjet-printed microfluidic RFID-enabled platform for wireless Lab-on-Chip applications," *IEEE Trans. Microw. Theory Techn.*, vol. 61, no. 12, pp. 4714–4723, Dec. 2013.
- [19] B. G. Colpitts and G. Boiteau, "Harmonic radar transceiver design: Miniature tags for insect tracking," *IEEE Trans. Antennas Propag.*, vol. 52, no. 11, pp. 2825–2832, Nov. 2004.
- [20] D. Mascanzoni and H. Wallin, "The harmonic radar: A new method of tracing insects in the field," *Ecological Entomol.*, vol. 11, no. 4, pp. 387–390, Nov. 1986.
- [21] J. R. Riley et al., "Tracking bees with harmonic radar," Nature, vol. 379, no. 6560, pp. 29–30, Jan. 1996.

- [22] X. Hui, Y. Ma, and E. C. Kan, "Code division multiple access in centimeter accuracy harmonic RFID locating system," *IEEE J. Radio Freq. Identificat.*, vol. 1, no. 1, pp. 51–58, Mar. 2017.
- [23] L. Zhu, N. Alkhaldi, H. M. Kadry, S. Liao, and P.-Y. Chen, "A compact hybrid-fed microstrip antenna for harmonics-based radar and sensor systems," *IEEE Antennas Wireless Propag. Lett.*, vol. 17, no. 12, pp. 2444–2448, Dec. 2018.
- [24] X. Gu, N. N. Srinaga, L. Guo, S. Hemour, and K. Wu, "Diplexer-based fully passive harmonic transponder for Sub-6-GHz 5G-compatible IoT applications," *IEEE Trans. Microw. Theory Techn.*, vol. 67, no. 5, pp. 1675–1687, May 2019.
- [25] B. Kubina, R. Jakoby, M. Schüßler, C. Mandel, and J. Romeu, "Quasichipless wireless temperature sensor based on harmonic radar," *Electron. Lett.*, vol. 50, no. 2, pp. 86–88, Jan. 2014.
- [26] D. Ahbe, S. Beer, T. Zwick, Y. Wang, and M. M. Tentzeris, "Dual-band antennas for frequency-doubler-based wireless strain sensing," *IEEE Antennas Wireless Propag. Lett.*, vol. 11, pp. 216–219, 2012.
- [27] C. Cho, X. Yi, D. Li, Y. Wang, and M. M. Tentzeris, "Passive wireless frequency doubling antenna sensor for strain and crack sensing," *IEEE Sensors J.*, vol. 16, no. 14, pp. 5725–5733, Jul. 2016.
- [28] A. Lazaro, R. Villarino, and D. Girbau, "A passive harmonic tag for humidity sensing," *Int. J. Antennas Propag.*, vol. 2014, Jul. 2014, Art. no. 670345.
- [29] A. Abdelnour, A. Lazaro, R. Villarino, D. Kaddour, S. Tedjini, and D. Girbau, "Passive harmonic RFID system for buried assets localization," *Sensors*, vol. 18, no. 11, p. 3635, Oct. 2018.
- [30] M. I. M. Ghazali, S. Karuppuswami, and P. Chahal, "Embedded passive RF tags towards intrinsically locatable buried plastic materials," in Proc. IEEE 66th Electron. Compon. Technol. Conf. (ECTC), May 2016, pp. 2575–2580.
- [31] S. Mondal *et al.*, "Monitoring and localization of buried plastic natural gas pipes using passive RF tags," *AIP Conf. Proc.*, vol. 1949, Apr. 2018, Art. no. 020020.
- [32] M. Hajizadegan et al., "Graphene sensing modulator: Toward low-noise, self-powered wireless microsensors," *IEEE Sensors J.*, vol. 17, no. 22, pp. 7239–7247, Nov. 2017.
- [33] X. Hui and E. C. Kan, "Monitoring vital signs over multiplexed radio by near-field coherent sensing," *Nature Electron.*, vol. 1, no. 1, pp. 74–78, Jan. 2018.
- [34] H. Huang et al., "Chemical-sensitive graphene modulator with a memory effect for Internet-of-Things applications," *Microsyst. Nanoeng.*, vol. 2, no. 1, p. 16018, Dec. 2016.
- [35] H. Y. Huang, M. Sakhdari, M. Hajizadegan, A. Shahini, D. Akinwande, and P.-Y. Chen, "Toward transparent and self-activated graphene harmonic transponder sensors," *Appl. Phys. Lett.*, vol. 108, no. 17, Apr. 2016, Art. no. 173503.
- [36] Y.-Y. Zheng, Y.-T. Ma, J.-Y. Zhang and X. Xie, "COVID-19 and the cardiovascular system," *Nature Rev. Cardiol.*, vol. 17, pp. 259–260, Mar. 2020.
- [37] H. Huang, P.-Y. Chen, C.-H. Hung, R. Gharpurey, and D. Akinwande, "A zero power harmonic transponder sensor for ubiquitous wireless μL liquid-volume monitoring," Sci. Rep., vol. 6, no. 1, May 2016, Art. no. 18795.
- [38] H. Huang, P.-Y. Chen, C.-H. Hung, R. Gharpurey, and D. Akinwande, "Frequency hopped wireless passive sensing system with harmonic transponder antenna sensor," in *IEEE MTT-S Int. Microw. Symp. Dig.*, May 2015, pp. 1–4.
- [39] V. Palazzi, F. Alimenti, P. Mezzanotte, G. Orecchini, and L. Roselli, "Zero-power, long-range, ultra low-cost harmonic wireless sensors for massively distributed monitoring of cracked walls," in *IEEE MTT-S Int. Microw. Symp. Dig.*, Honolulu, HI, USA, Jun. 2017, pp. 1335–1338.
- [40] L. Zhu and P.-Y. Chen, "A compact, zero-power and low-noise harmonic-transponder for liquid and moisture sensing," in *Proc. IEEE Int. Symp. Antennas Propag. USNC-URSI Radio Sci. Meeting*, Atlanta, GA, USA, USA, Jul. 2019, pp. 1109–1110.
- [41] L. Zhu, M. Farhat, Y.-C. Chen, K. N. Salama, and P.-Y. Chen, "A compact, passive frequency-hopping harmonic sensor based on a microfluidic reconfigurable dual-band antenna," *IEEE Sensors J.*, early access, Jun. 8, 2020, doi: 10.1109/JSEN.2020.3000778.
- [42] A. Erentok and R. W. Ziolkowski, "Metamaterial-inspired efficient electrically small antennas," *IEEE Trans. Antennas Propag.*, vol. 56, no. 3, pp. 691–707, Mar. 2008.
- [43] R. W. Ziolkowski and A. Erentok, "Metamaterial-based efficient electrically small antennas," *IEEE Trans. Antennas Propag.*, vol. 54, no. 7, pp. 2113–2130, Jul. 2006.

- [44] R. W. Ziolkowski, P. Jin, and C.-C. Lin, "Metamaterial-inspired engineering of antennas," *Proc. IEEE*, vol. 99, no. 10, pp. 1720–1731, Oct. 2011.
- [45] R. Fleury, J. Soric, and A. Alù, "Physical bounds on absorption and scattering for cloaked sensors," *Phys. Rev. B*, vol. 89, no. 4, Jan. 2014, Art. no. 045122.
- [46] P.-Y. Chen, H. Huang, and C.-H. Hung, "Compact metamaterial-enclosed wireless sensors with subtle perception of internal physical events," *Appl. Phys. Lett.*, vol. 107, no. 19, Nov. 2015, Art. no. 194101.
- [47] P. Y. Chen and A. Alu, "Dual-mode miniaturized elliptical patch antenna with μ-negative metamaterials," *IEEE Antennas Wireless Propag. Lett.*, vol. 9, pp. 351–354, 2010.
- [48] P. Y. Chen and A. Alu, "Sub-wavelength elliptical patch antenna loaded with μ-negative metamaterials," *IEEE Trans. Antennas Propag.*, vol. 58, no. 9, pp. 2909–2919, Sep. 2010.
- [49] ANSYS 2020 R1 Academic Research Electromagnetics Suite, ANSYS, Inc., Canonsburg, PA, USA, 2020.
- [50] Keysight PathWave Advanced Design System (ADS), Keysight Technol., Santa Rosa, CA, USA, 2020.
- [51] VLF-1525+ From Mini-Circuit. Accessed: Jan. 10, 2020. [Online]. Available: https://www.minicircuits.com/WebStore/dashboard.html? model=VLF-1525%2B
- [52] VHF-1810+ From Mini-Circuit. Accessed: Jan. 10, 2020. [Online]. Available: https://www.minicircuits.com/WebStore/dashboard.html? model=VHF-1810
- [53] K. Saeed, R. D. Pollard, and I. C. Hunter, "Substrate integrated waveguide cavity resonators for complex permittivity characterization of materials," *IEEE Trans. Microw. Theory Techn.*, vol. 56, no. 10, pp. 2340–2347, Oct. 2008.
- [54] J. A. Shaw, "Radiometry and the friis transmission equation," Amer. J. Phys., vol. 81, no. 1, pp. 33–37, Jan. 2013.
- [55] C. Gao, T. Wei, F. Duewer, Y. Lu, and X.-D. Xiang, "High spatial resolution quantitative microwave impedance microscopy by a scanning tip microwave near-field microscope," *Appl. Phys. Lett.*, vol. 71, no. 13, pp. 1872–1874, Sep. 1997.
- [56] H. Huang et al., "RFID tag Helix antenna sensors for wireless drug dosage monitoring," IEEE J. Transl. Eng. Health Med., vol. 2, no. 1700108, pp. 1–8, Mar. 2014.



Liang Zhu (Graduate Student Member, IEEE) received the M.Sc. degree in optics from Sun Yat-sen University, Guangzhou, China, in 2015. He is currently pursuing the Ph.D. degree in electrical engineering at the University of Illinois at Chicago, Chicago, IL, USA.

His research mainly focuses on RF/microwave antennas and circuits, energy harvesting platforms, and wireless sensors.



**Haiyu Huang** (Member, IEEE) received the Ph.D. degree from The University of Texas at Austin, Austin, TX, USA, in 2014.

He was a Research Staff with the Houston Methodist Hospital Research Institute, Houston, TX, USA, from 2010 to 2013, and a Research Assistant with The University of Texas Health Science Center at Houston, Houston, TX, from 2009 to 2010. He is currently a Technical Staff Principal Member with Maxim Integrated Inc., Dallas, TX, USA. He has more than 30 publications in peer-reviewed journals

and conference proceedings, as well as more than 10 U.S. and international patents. He has been involved in the research and development of applied machine learning for sensors and communications, integrated RF and wireless SoC products for Internet-of-Things (IoTs), and miniaturized wireless sensors for healthcare applications.

Dr. Huang was a recipient of the National Science Foundation (NSF) Healthcare Innovation Award.



Mark Ming-Cheng Cheng received the B.S. and Ph.D. degrees from National Tsing-Hua University, Hsinchu, Taiwan, in 1995 and 2003, respectively.

He was a NIH Post-Doctoral Fellow with the Heart and Lung Research Institute, The Ohio State University, Columbus, OH, USA, from 2003 to 2005. He was a Research Assistant Professor with the Department of Nanomedicine and Biomedical Engineering, The University of Texas Health Science Center at Houston, Houston, TX, USA, from 2006 to 2007. In 2008, he joined Wayne State University

(WSU) and became a Full Professor in 2019. At WSU, he initialized curriculum in Nanoengineering and Cyber-Physical Systems (CPS). In 2019, he joined the Department of Electrical and Computer Engineering, The University of Alabama, Tuscaloosa, AL, USA, where he is currently a Professor. He has authored approximately 120 articles in peer-reviewed journal and conference proceedings. He has been involved in multidisciplinary research in microsystem design, biomedical devices, biosensors, new materials, wearable sensors, and environmental Internet-of-Things (IoT).

Dr. Cheng was a recipient of the National Science (NSF) CAREER Award, the ONR Summer Faculty Fellowship, and the President Research Enhancement Award.



**Pai-Yen Chen** (Senior Member, IEEE) received the Ph.D. degree from The University of Texas at Austin, Austin, TX, USA, in 2013.

He was a Research Staff with the National Nano Device Laboratory, Hsinchu, Taiwan, from 2006 to 2009, and a Research Scientist with the Metamaterial Commercialization Center, Intellectual Ventures, Bellevue, WA, USA, from 2013 to 2014. He is currently an Associate Professor with the Department of Electrical and Computer Engineering, University of Illinois at Chicago, Chicago, IL, USA.

He has authored approximately 95 peer-reviewed articles, 100 conference proceedings, 1 book, 8 book chapters, and 10 U.S. patents. He has been involved in multidisciplinary research on applied electromagnetics, wireless microsensors/nanosensors and integrated systems, innovative RF antennas and circuits, metamaterials, as well as nano-electromagnetism in plasmonics and nanophotonics.

Dr. Chen was a recipient of the National Science Foundation (NSF) CAREER Award, the IEEE Sensors Council Young Professional Award, the IEEE Raj Mittra Travel Grant (RMTG) Award, the SPIE Rising Researcher Award, the ACES Early Career Award, the Young Scientist Awards from PIERS, URSI General Assembly, and URSI Commission B: Electromagnetics, the Air Force Research Laboratory Faculty Fellowship, the College of Engineering Faculty Research Excellence Award, the Donald Harrington Fellowship, the University of Texas Professional Development Award, the Taiwan Ministry of Education Study Abroad Award, the United Microelectronics Corporation Scholarship, and quite a few student paper awards and travel grants from major IEEE conferences, including the USNC-URSI Ernest K. Smith Student Paper Award. He currently serves as an Associate Editor for the IEEE SENSORS JOURNAL, the IEEE JOURNAL OF RADIO FREQUENCY IDEN-TIFICATION (IEEE JRFID), the IEEE JOURNAL OF ELECTROMAGNETICS, RF AND MICROWAVES IN MEDICINE AND BIOLOGY (IEEE-JERM), and a Guest Editor for several international journals. He was a former Associate Editor of the Applied Electromagnetics.